

Oxygen self-diffusion mechanisms in monoclinic ZrO_2 revealed and quantified by density functional theory, random walk analysis, and kinetic Monte Carlo calculations

Jing Yang,¹ Mostafa Youssef,^{1,2,*} and Bilge Yildiz^{1,2,†}

¹Laboratory for Electrochemical Interfaces, Department of Materials Science and Engineering, Massachusetts Institute of Technology, 77 Massachusetts Avenue, Cambridge, Massachusetts 02139, USA

²Department of Nuclear Science and Engineering, Massachusetts Institute of Technology, 77 Massachusetts Avenue, Cambridge, Massachusetts 02139, USA



(Received 22 August 2017; published 29 January 2018)

In this work, we quantify oxygen self-diffusion in monoclinic-phase zirconium oxide as a function of temperature and oxygen partial pressure. A migration barrier of each type of oxygen defect was obtained by first-principles calculations. Random walk theory was used to quantify the diffusivities of oxygen interstitials by using the calculated migration barriers. Kinetic Monte Carlo simulations were used to calculate diffusivities of oxygen vacancies by distinguishing the threefold- and fourfold-coordinated lattice oxygen. By combining the equilibrium defect concentrations obtained in our previous work together with the herein calculated diffusivity of each defect species, we present the resulting oxygen self-diffusion coefficients and the corresponding atomistically resolved transport mechanisms. The predicted effective migration barriers and diffusion prefactors are in reasonable agreement with the experimentally reported values. This work provides insights into oxygen diffusion engineering in ZrO_2 -related devices and parametrization for continuum transport modeling.

DOI: [10.1103/PhysRevB.97.024114](https://doi.org/10.1103/PhysRevB.97.024114)

I. INTRODUCTION

Oxygen self-diffusion in zirconium oxide has long been a topic of interest [1–4] in studying the oxidation kinetics of zirconium alloys, which are used as cladding of nuclear fuel in light water cooled nuclear reactors [5]. Zirconium oxide is also widely used in heterogeneous catalysis [6,7], and more recently it was examined for high- k dielectrics in metal-oxide-semiconductor field-effect transistor (MOSFET) devices [8,9] as well as resistive switching devices [10,11]. In all of these technologically important applications, understanding the defect chemistry and transport properties is key to better material design, device engineering, and performance modeling. In particular, such knowledge could guide design by, e.g., aliovalent doping and controlling operating environmental conditions. Experimental [12–14] and computational [15–20] studies have been carried out to atomistically resolve the structure, valence states, and defect chemistry in ZrO_2 . Zirconium-oxygen system phase stability has been examined by first-principles studies, and a range of suboxide structures with oxygen dissolved into the metal phase have been identified [20]. To date, many aspects of ZrO_2 remain unexamined atomistically in the multidimensional space of temperature, oxygen partial pressure, extrinsic doping, strain, and microstructure. In our previous work, we predicted oxygen self-diffusion kinetics in tetragonal- ZrO_2 (t - ZrO_2) by combining

first-principles calculations with random walk theory [21], resulting in good agreement with experimental measurements. Monoclinic- ZrO_2 (m - ZrO_2) is the stable phase below 1440 K [22] and is also relevant in the applications mentioned above. In m - ZrO_2 , the oxygen sublattice is distorted compared to the tetragonal phase, leading to two inequivalent sites for oxygen in the unit cell: one bonds with four zirconium atoms (O4) and one bonds with three zirconium atoms (O3). This inequivalence of oxygen sites makes the random walk model inapplicable. There exist first-principles studies of oxygen defect migration barriers in HfO_2 , which bears the same structure as m - ZrO_2 [23]. However, no comprehensive work predicting overall oxygen diffusion coefficients has been performed for oxides of this structure.

In this study, we present a systematic examination of oxygen transport properties in bulk, near-stoichiometric monoclinic ZrO_2 under different thermodynamic conditions. In previous work, by combining first-principles-based point-defect calculations with statistical thermodynamics, we were able to predict equilibrium defect concentrations at various temperatures and oxygen partial pressures both in tetragonal [24] and monoclinic ZrO_2 [16]. Here we calculated the migration barriers of different oxygen defect types and migration paths by first-principles calculations. The results show that migration barriers corresponding to different oxygen vacancy migration paths categorized by O4 and O3 sites could differ by more than 1 eV. To distinguish this inequivalence of lattice oxygen sites, we quantified the oxygen vacancy diffusivity with kinetic Monte Carlo (kMC) simulations. On the other hand, random walk theory was sufficient to obtain the oxygen interstitial diffusivities. We arrive at the total oxygen self-diffusion coefficients by combining the defect equilibria and diffusivity for each of these oxygen defects

*Present address: Department of Mechanical Engineering, The American University in Cairo, AUC Avenue, P.O. Box 74, New Cairo 11835, Egypt.

†Author to whom all correspondence should be addressed: byildiz@mit.edu

over a wide range of temperature and oxygen partial pressure.

The predicted diffusion coefficient profiles show a valley shape as a function of oxygen pressure at different temperatures. The oxygen interstitial dominates in the high oxygen partial pressure regime, and the oxygen vacancy dominates in the low oxygen partial pressure regime, leading to a diffusion minimum at intermediate oxygen partial pressures. Our predicted values are in good agreement with experimentally measured diffusion coefficients under relevant thermodynamic conditions. Finally, we discuss the implications of this study on engineering oxygen transport in zirconium oxide.

II. METHODS

The climbing image nudged elastic band (CI-NEB) method [25] was used to calculate migration barriers using three to five intermediate images as implemented in Transition State Tools (VTST) [25]. The energies of each image were calculated using density functional theory (DFT) with Vienna Ab initio Simulation Package (VASP) [26–29] with a $2 \times 2 \times 2$ supercell and a $2 \times 2 \times 2$ k -point grid. The generalized gradient approximation (GGA) with a Perdew-Burke-Ernzerhof (PBE) functional [30,31] is used. $4s^2 4p^6 4d^2 5s^2$ electrons for zirconium and $2s^2 2p^4$ for oxygen are treated as valence electrons. The plane-wave cutoff energy was set to 450 eV. Details of calculating the defect formation energies and equilibrium defect concentrations can be found in Refs. [24,16,32].

For oxygen interstitials, DFT calculations were performed with different initial guesses for the interstitial sites. Oxygen vacancies can take either O4 or O3 sites. On the other hand, the interstitial oxygen always occupies the same type of site in the relaxed, low-energy configurations. This finding validates the applicability of the random walk theory for oxygen interstitials, as we reported earlier for oxygen diffusion in t -ZrO₂ [21]. In principle, random walk theory produces the same outcome as kinetic Monte Carlo simulations for oxygen interstitials, given that there are no inequivalent sites for them in m -ZrO₂. Therefore, the diffusivity for each oxygen interstitial species was calculated by the random walk model [33] with

$$D_{O_i}^q = \sum_k \nu d_k^2 \exp\left(-\frac{E_k}{k_B T}\right), \quad (1)$$

where the attempt frequency ν is taken as 5 THz. q represents the different charged states of oxygen interstitials (0, -1 , and -2). E_k and d_k are the migration barrier and hopping distance for the corresponding migration path. k_B is the Boltzmann constant and T is the temperature. Kröger-Vink notation for defects is used throughout this paper.

The calculated migration barriers for oxygen vacancies were fed into an on-lattice kinetic Monte Carlo model [34] to account for the threefold- and fourfold-coordinated oxygen site network. Simulations were performed at each temperature for 10^6 kMC steps. The simulation cell has one defect in the ZrO₂ lattice with a periodic boundary condition, starting from a random initial configuration. The diffusivity is calculated from the mean-square displacement with Einstein's theory of Brownian motion [35],

$$\langle \mathbf{r}(t)^2 \rangle = 6D_{V_o}^q t. \quad (2)$$

Here $\mathbf{r}(t)$ is the position of the defect referenced to the initial site at time t , and $D_{V_o}^q$ is the calculated diffusivity for the specific defect species V_o^q at that temperature. The calculation of $D_{V_o}^q$ from the kMC trajectory involves the following. For each defect species, one trajectory of N steps is obtained from the kMC run. This single trajectory is broken into N/n trajectories with n steps. For each n -step trajectory, an associated diffusivity D_n is calculated by $D_n = \Delta r_n^2 / 6t_n$, where Δr_n^2 represents the total mean-squared displacement of this trajectory, and t_n represents the total time. Due to the nature of kMC, t_n is different for each n -step trajectory. The final diffusivity is calculated by averaging D_n from the (N/n) trajectories. In this work, $N = 10^6$ and $n = 5 \times 10^3$ were used. Convergence of the simulations with these parameters is shown in the Supplemental Material [36]. Defect-defect interactions are ignored in all calculations under the assumption of a dilute limit, which is reasonable for undoped monoclinic ZrO₂, which does not exhibit significant deviation from stoichiometry [16,37].

By combining the contribution to diffusion by oxygen vacancies from kMC calculations and by oxygen interstitials from random walk theory, we obtain the total oxygen self-diffusion coefficient at different partial pressures and temperatures,

$$D_{\text{tot}} = \sum_q [V_o^q] D_{V_o}^q + \sum_q [O_i^q] D_{O_i}^q. \quad (3)$$

Here $[d]$ is the concentration of respective defect. D_{tot} defined here is the isotropic diffusion coefficient of oxygen averaged over all crystallographic directions. This value is then compared with experimental values in Sec. III.

III. RESULTS AND DISCUSSION

The considered pathways of oxygen vacancy migration are shown schematically in Fig. 1. Two types of oxygen sites exist in monoclinic ZrO₂, one type bonded with four zirconium ions (O4) and the other with three (O3). The migration paths

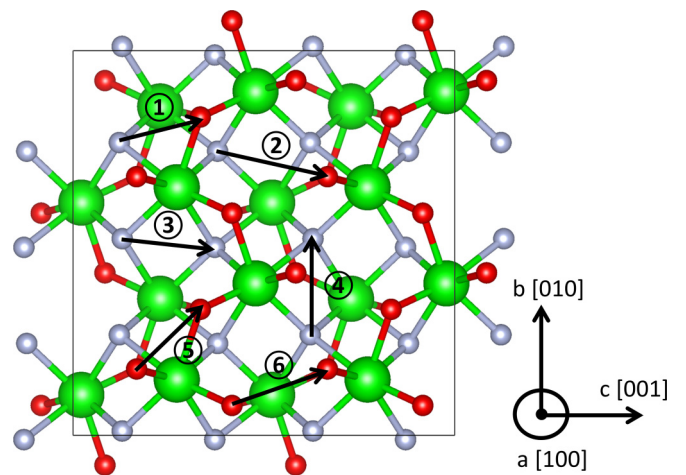


FIG. 1. Migration paths for oxygen vacancies in m -ZrO₂. Large, green spheres represent Zr ions. Small red and gray spheres represent threefold-coordinated and fourfold-coordinated oxygen ions, respectively. This figure is generated with visualization software VESTA [38].

TABLE I. The calculated migration paths and migration barriers (in units of eV) of oxygen vacancies in *m*-ZrO₂. The indices of each migration path are labeled in Fig. 1. The paths are categorized by O4 and O3 oxygen sites, and how many Zr ions the two O sites share a bond with. For paths between O4 and O3 sites, forward and backward barriers are different due to asymmetry of the initial and final configuration. For O4-O4 and O3-O3 paths, forward and backward barriers are equal. For O4-O4 paths, migration on the *ab* plane and the *c* direction are further distinguished.

Path	From-To	Shared Zr ion		V_O^\times	V_O^\bullet	$V_O^{\bullet\bullet}$
1	O4-O3	2	forward	1.94	0.91	0.06
			backward	1.84	1.28	0.78
2	O4-O3	1	forward	2.23	1.64	1.01
			backward	2.12	2.00	1.80
3	O4-O4, <i>c</i>	2		2.48	1.54	0.86
4	O4-O4, <i>ab</i>	2		2.03	1.20	0.33
5	O3-O3	2		2.20	1.58	0.77
6	O3-O3	1		1.32	1.11	0.73

are further categorized by the number of zirconium ions that simultaneously share bonds with the two oxygen sites between which the migration takes place. The details of each migration path and the corresponding migration barriers are summarized in Table I, and the energy profiles are shown in Fig. 2. For each migration path, the barrier for oxygen vacancies with 0, +1, and +2 charges are calculated.

Based on the calculated migration barrier, it is clear that for each migration path, the higher-charge-state oxygen vacancies have lower migration barriers. This can be rationalized by the fact that the diffusive jump of V_O^\times involves the transport of the two electrons associated with the vacant site in a direction opposing the jump of the oxide ion. This opposition

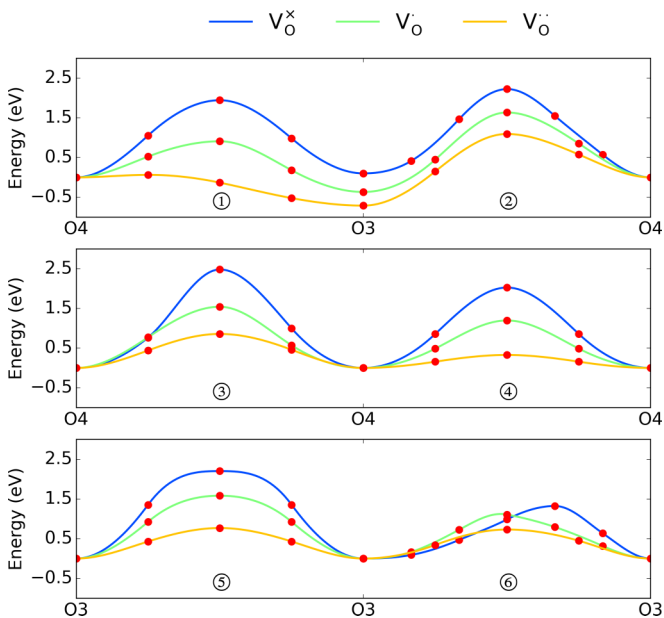


FIG. 2. Energy profiles for oxygen migration paths labeled in Fig. 1. Red dots are images calculated using the CI-NEB method. Fitted spline curves are produced with the VTST tools [25].

is accompanied by Coulombic repulsion and elevation of the activation barrier. In the case of V_O^\bullet , there is only one electron opposing the migrating oxide ion, and finally in $V_O^{\bullet\bullet}$ there are no electrons to oppose the oxide ion. A similar trend has also been observed in tetragonal ZrO₂ [21] and other oxides [39]. It is also notable that the forward migration barrier for O4-O3 sharing bonds with Zr ions is as low as 0.06 eV, which seemingly indicates very fast oxygen diffusion. However, it is shown from kMC simulations that, although oxygen hopping between these two types of sites is frequent, oxygen atoms need to go through other high-barrier migration paths in order to complete long-range diffusion.

For oxygen interstitials, octahedral interstitial sites were found to be the low-energy sites [16]. DFT calculations show that all octahedral oxygen interstitials are energetically equivalent in the ZrO₂ unit cell. Migration barriers for the direct exchange mechanism were found to be too high (>5 eV) and therefore only interstitialcy migration hops were considered [23]. The calculated migration barriers are 0.672, 0.365, and 0.530 eV, respectively, for O_i^\times , O_i' , and O_i'' . These results indicate that oxygen interstitials have higher mobility compared to oxygen vacancies, consistent with previous experimental observation [1].

Equilibrium defect concentrations as a function of P_{O_2} at 600 and 1200 K are reproduced in Figs. 3(a) and 3(b). Details of how these profiles are constructed can be found in Ref. [16]. At 600 K, the dominant oxygen-related defect is oxygen interstitial over the entire P_{O_2} range, with the dominant charge state changing from -2 to 0 at 1 atm. At 1200 K, the dominant oxygen defect transitions from an oxygen vacancy with different charge states for $P_{O_2} < 10^{-12}$ atm to a doubly charged oxygen interstitial O_i'' at higher, more oxidizing P_{O_2} .

The total oxygen self-diffusivity profiles as well as contributions of individual oxygen defect species at the two temperatures display different features [Figs. 3(c) and 3(d)], following the defect transitions noted above. In the low-temperature case, P_{O_2} dependence can be categorized into two regimes. In the low P_{O_2} regime ($< 10^{-20}$ atm), the dominant charged defects are holes compensated by electrons. This results in a $1/2$ slope for the concentration of the dominant oxygen defect O_i'' , and consequently the same slope for the $\log_{10} D_{tot}$ profile. In the high P_{O_2} regime ($> 10^{-10}$ atm), holes are charge-balanced by zirconium vacancies V_{Zr}'''' . Here the defect reaction is $\frac{1}{2}O_2(g) \rightarrow O_O^\times + \frac{1}{2}V_{Zr}'''' + 2h^\bullet$, leading to $[h^\bullet] = \frac{1}{4}[V_{Zr}''''] \propto P_{O_2}^{1/5}$. The concentration of O_i'' is related to $[h^\bullet]$ via the defect reaction $\frac{1}{2}O_2(g) \rightarrow O_i'' + 2h^\bullet$ and thus exhibits the $1/10$ slope as shown in the $\log_{10} D_{tot}$ curve.

At high temperature, the intermediate P_{O_2} regime ($10^{-15} - 10^{-10}$ atm) has the same electron-hole compensation mechanism and the same dominant oxygen defect O_i'' as discussed above, and thus, $\log_{10} D_{tot}$ exhibits $1/2$ slope. However, in the low P_{O_2} regime, the two dominating types of charged defect are electrons and positively charged oxygen vacancies. A $-1/6 \log_{10} D_{tot}$ slope is predicted by the law of mass action under the approximate charge neutrality $n_c \approx 2[V_O^{\bullet\bullet}]$, but a small discrepancy from this prediction was present in the calculated curve. This is because V_O^\bullet also contributes non-negligibly to the charge-neutrality condition. At very low P_{O_2} , V_O^\bullet and V_O^\times predominate over $V_O^{\bullet\bullet}$ in concentration,

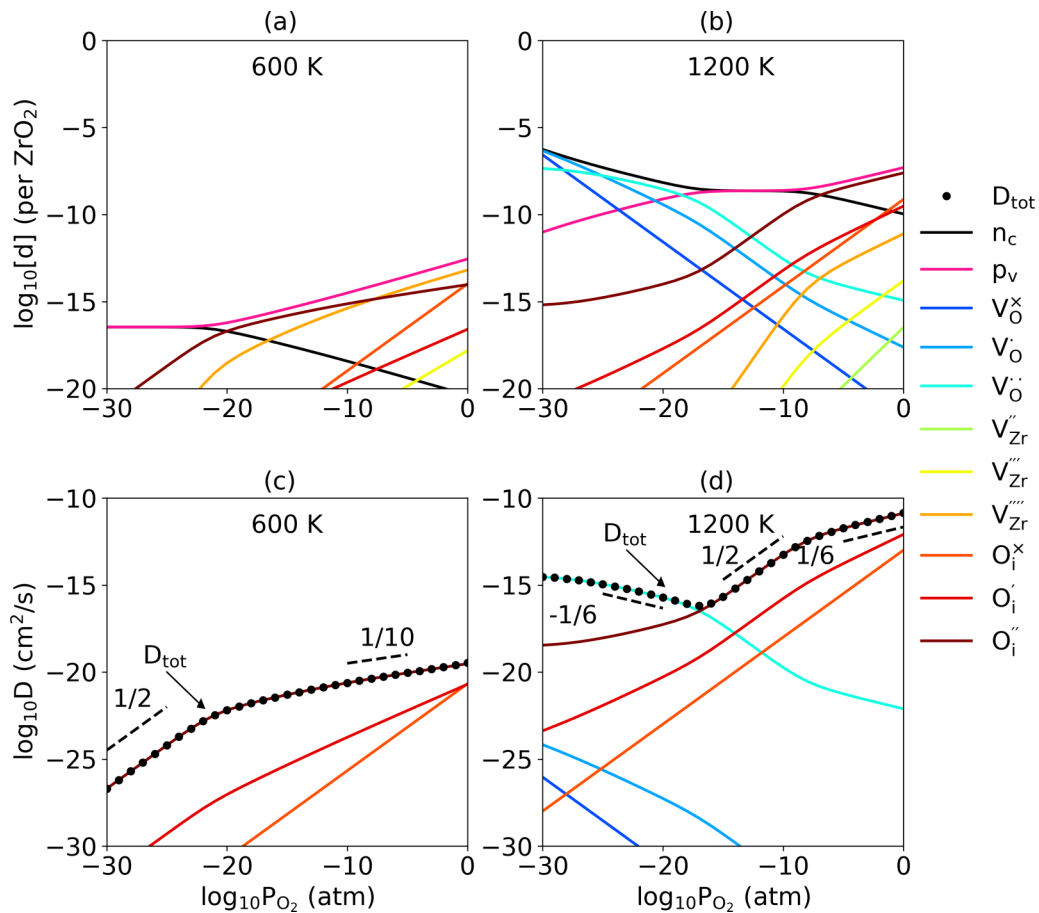


FIG. 3. Equilibrium concentrations of electronic and ionic defects, $[d]$ at (a) 600 K and (b) 1200 K, as a function of oxygen partial pressure. Oxygen self-diffusivity, D , calculated for each oxygen defect species and total diffusion coefficient, D_{tot} , with varying oxygen partial pressure at (c) 600 K and (d) 1200 K.

but the diffusivity is still contributed mainly by V_{O}^{\bullet} due to its lower migration barrier. In the high P_{O_2} regime, $p_v \approx 2[O_i^{\prime\prime}]$. $\frac{1}{2}\text{O}_2(\text{g}) \rightarrow O_i^{\prime\prime} + 2h^{\bullet}$ is the dominant defect reaction, and a 1/6 slope is shown as predicted by the law of mass action.

To examine the gradual transition from the low-temperature behavior to the high-temperature behavior, we plot the P_{O_2} dependence of the total self-diffusion coefficient at different temperatures in Fig. 4(a). There is a clear appearance of a diffusion coefficient minima, or valley, as marked by the dashed line. This marks the transition from the V_{O}^{\bullet} -dominated regime to the $O_i^{\prime\prime}$ -dominated regime. At low temperatures (<700 K), the entire P_{O_2} range is dominated by oxygen interstitials. At higher temperatures, there is a transition between the V_{O}^{\bullet} -dominated regime at low P_{O_2} and the $O_i^{\prime\prime}$ -dominated regime at high P_{O_2} . The oxygen partial pressure at which this transition occurs increases with increasing temperature.

To compare with experiments, the high-temperature data are replotted in Fig. 4(b) as isobaric diffusion coefficient curves as a function of $1/T$. At high P_{O_2} ($>10^{-5}$ atm), the isobaric curves are perfectly Arrhenius. This is because the entire profile is sampled in regimes where oxygen interstitials are compensated by holes. At intermediate P_{O_2} ($10^{-10} - 10^{-5}$ atm), non-Arrhenius behavior starts to appear, where the compensation mechanism transitions to electrons compensated by holes.

At even lower P_{O_2} , the Arrhenius behavior is restored again because now the entire region is within the vacancy-dominated regime.

Symbols in Fig. 4(b) represent experimentally measured values at different oxygen partial pressures as noted in the legend [1–3]. It is clear from Fig. 4(b) that experimental measurements have considerable disagreement between each other. In particular, the trend of D_{tot} varying with oxygen partial pressure is not consistent when comparing values from different studies. Here we discuss a few factors that may lead to this discrepancy. First, all experimental studies listed here were not conducted on single-crystal ZrO_2 . References [1] and [2] measured conductivity via an ^{18}O diffusion experiment on ZrO_2 spheres, and Ref. [3] by measuring the oxidation rate of nonstoichiometric ZrO_2 powder to stoichiometric ZrO_2 . It is hard to eliminate the contribution of voids, grain boundaries, or other types of extended defects. Second, all diffusion models used to fit experimental profiles and obtain D_{tot} assume that the rate-limiting step in the oxygen exchange/oxidation process is oxygen diffusion. This simplified assumption may lead to errors in the fitted result. This point is partially verified by Ref. [1], where the authors found that diffusivities obtained at equivalent oxygen partial pressure by CO/CO_2 mixture and O_2 gas are not consistent, indicating that surface exchange kinetics also influences the result. Third, none of these studies considers

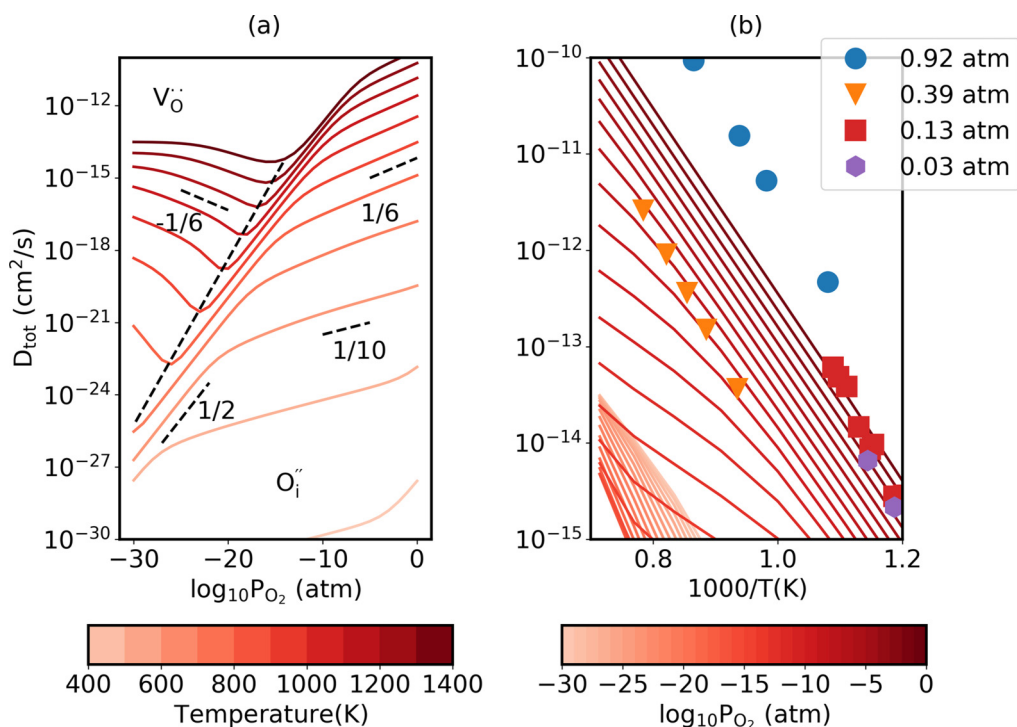


FIG. 4. Calculated total oxygen self-diffusion coefficient plotted as a function of oxygen partial pressure and temperature. Dotted lines in (b) show experimentally measured values from Refs. [1] (0.92 atm), [2] (0.39 atm), and [3] (0.13 and 0.03 atm).

the contribution to oxygen diffusion under an electric field in an intrinsically formed space-charge layer at the oxide surface. Our study shows that the major contribution to the diffusion coefficient comes from charged defects, and the space-charge effect should be taken into consideration [32].

Lastly, it is worth mentioning that experimental specimens must contain aliovalent cation impurities. For example, Al³⁺ and Nb⁵⁺ are two common impurity species; one is an acceptor and the other is a donor. These aliovalent cations could compensate for each other and make the oxide behave closer to intrinsic. However, even a small amount of *n*-type or *p*-type doping could change the dependence of defect chemistry to

oxygen partial pressure. In particular, the compensating mechanism transition pressure could change due to the impurity dopants. In other words, the same defect chemistry could be achieved at different P_{O_2} with different impurity contents. This could explain in part the inconsistency of the P_{O_2} dependence between prior experimental studies. The trend in diffusivity change from 0.03 to 0.13 atm in Ref. [3] is more reliable considering the measurements were performed on samples with the same impurity level. In Ref. [3] we see that D_{tot} increases with oxygen partial pressure, which hints at an oxygen-interstitial-dominated mechanism and is in agreement with our prediction.

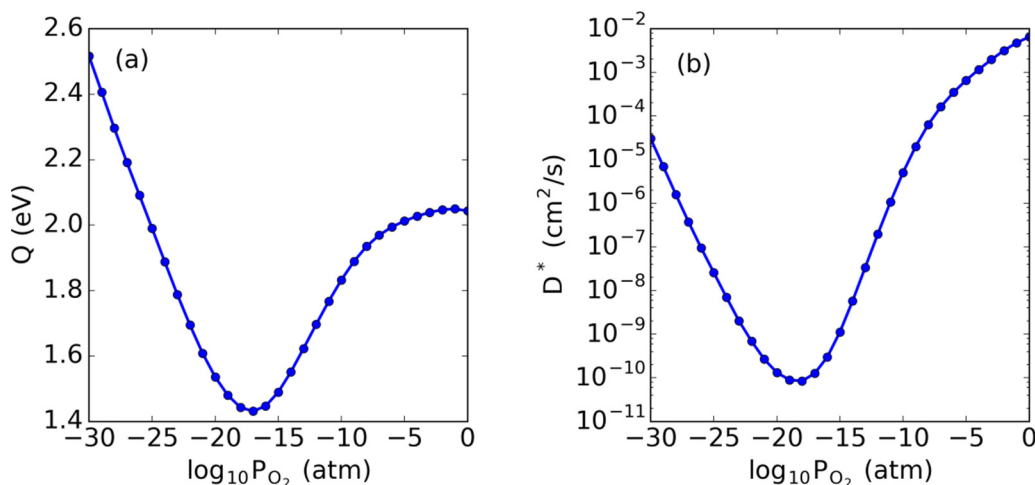


FIG. 5. (a) Activation energies and (b) diffusion prefactors at different oxygen partial pressures fitted to $D_{tot} = D^* \exp(-Q/k_B T)$ by using the simulated data in the high-temperature regimes in Fig. 4(b).

TABLE II. Activation energy and diffusion prefactor comparison between this work and experimental measurements.

	This work	This work	This work	Ref. [1]	Ref. [2]	Ref. [3]	Ref. [3]
P_{O_2} (atm)	1	0.1	0.01	0.92	0.39	0.13	0.03
Q (eV)	2.04	2.05	2.05	1.96	2.43	2.46	2.46
D^* (cm ² /s)	6.50×10^{-3}	4.76×10^{-3}	3.16×10^{-3}	2.34×10^{-2}	9.73×10^{-3}	1.82	9.00×10^{-2}

To compare quantitatively with experimentally measured values, we calculate the effective activation energies Q and effective prefactors D^* by fitting the total self-diffusivity D_{tot} to $D_{\text{tot}} = D^* \exp(-Q/k_B T)$. The outcome values are plotted in Fig. 5 and summarized in Table II. It is not a coincidence that both the activation energy and the diffusion prefactor curves display a valley at intermediate oxygen partial pressure. This valley again corresponds to the same transition from the V_{O}^{\bullet} -dominated regime at low P_{O_2} to the O_i'' -dominated regime at high P_{O_2} . The effective activation barrier predicted at $P_{O_2} = 1$ atm is 2.04 eV. This is in reasonable agreement with experimentally measured values (1.96 eV [1], 2.43 eV [2], and 2.46 eV [3], respectively). This consistency indicates that all the values we are comparing with from experiments should be in the same O_i'' -dominated regime as we predicted. This is because the formation energy of V_{O}^{\bullet} alone exceeds 3.5 eV in this P_{O_2} range, and an even higher activation barrier should be expected if V_{O}^{\bullet} were the dominant species. When it comes to diffusion prefactors, the difference between this work and experimental values, and the difference among the reported experimental values, is more pronounced. D^* predicted in this study is 6.50×10^{-3} cm²/s at $P_{O_2} = 1$ atm and 4.76×10^{-3} cm²/s at $P_{O_2} = 0.1$ atm. The calculated values in Refs. [1–3] are 2.34×10^{-2} cm²/s at 0.92 atm, 9.73×10^{-3} cm²/s at 0.39 atm, 1.82 cm²/s at 0.13 atm, and 9.00×10^{-2} cm²/s at 0.03 atm. However, we can also see from Fig. 5(b) that D^* changes over orders of magnitude with varying oxygen partial pressures. This observation is consistent with the different impurity argument we discussed above. Acceptor-type impurity could increase the concentration of O_i'' and hence create the discrepancies among D^* .

Lastly, we comment on the implication of these findings on the oxidation rate of zirconium metal. Oxygen diffusion through the oxide passive film is known as one of the rate-limiting steps in the oxidation process [40]. To design corrosion-resistant zirconium alloys, lower oxygen diffusivity is desirable. Looking at the isothermal curves in Fig. 4(a), the lowest oxygen diffusion coefficient is always achieved in an intermediate pressure range where the dominating species are electrons and holes. Going to the high (low) end of oxygen partial pressure, the oxygen interstitial (oxygen vacancy) becomes the dominant defect species that compensates with holes (electrons), and thus increases total oxygen conductivity. This leads to the conclusion that, to engineer oxygen transport through the oxide film, it is desirable to suppress the dominant oxygen defect. Doping is one of the possible means to achieve this goal. In the high P_{O_2} region, a +3 dopant could compensate with the hole, reducing the oxygen interstitial concentration and thus suppressing oxygen transport. A +5 dopant has a similar effect in the low P_{O_2} region in compensating with

electrons and reducing oxygen vacancy. This finding provides guiding rules for different alloying elements that can dissolve into the growing oxide and change the oxygen defect equilibria in the relevant temperature and oxygen partial pressure space.

In light of our findings, we offer a few possible improvements on the modeling method used in this work. First, we ignored defect-defect interactions throughout this study. If we look at Fig. 3(b), the calculated defect concentrations are generally below 10 ppm, which shows that this approximation is reasonable within the thermodynamic regime considered here. However, if a high concentration of extrinsic doping or a higher temperature and lower oxygen pressure regime is of interest, it will be important to include defect-defect interactions. Second, extended defects in the oxide structure can significantly change its transport properties, as we have demonstrated recently, for example, for secondary phase particles embedded in a ZrO₂ matrix [32]. The effects of surface, grain boundaries, and interfaces on oxygen diffusion are also worth exploring, and this is necessary for constructing accurate higher-level transport models as well as informing microstructure engineering for oxide materials.

IV. CONCLUSION

In this study, we modeled oxygen self-diffusion in monoclinic-ZrO₂ by combining density functional theory calculations, random walk theory, and kinetic Monte Carlo simulations. The oxygen diffusion coefficient shows a clear transition from an oxygen-vacancy-dominated transport regime at low oxygen partial pressure to an oxygen-interstitial-dominated regime at high oxygen partial pressures. The results demonstrate a diffusivity minimum, i.e., a valley at the transition point. The effective migration barriers and diffusion prefactors are in reasonable agreement with those found from experimental studies. This study provides an atomistic understanding of the oxygen diffusion mechanism in monoclinic ZrO₂, and the findings can guide the design of zirconium oxide for different applications in which oxygen transport properties at different functional conditions are of interest.

ACKNOWLEDGMENTS

This work is supported by the Consortium for Advanced Simulation of Light Water Reactors (CASL), an Energy Innovation Hub for Modeling and Simulation of Nuclear Reactors under U.S. Department of Energy Contract No. DE-AC05-00OR22725. We acknowledge the Extreme Science and Engineering Discovery Environment (XSEDE) program for calculations performed under allocation No. TG-DMR120025.

- [1] F. J. Keneshea and D. L. Douglass, *Oxid. Met.* **3**, 1 (1971).
- [2] A. Madeyski and W. W. Smeltzer, *Mater. Res. Bull.* **3**, 369 (1968).
- [3] S. Aronson, *J. Electrochem. Soc.* **108**, 312 (1961).
- [4] U. Brossmann, R. Würschum, U. Södervall, and H.-E. Schaefer, *J. Appl. Phys.* **85**, 7646 (1999).
- [5] A. T. Motta, A. Couet, and R. J. Comstock, *Annu. Rev. Mater. Res.* **45**, 311 (2015).
- [6] K. T. Wan, C. B. Khouw, and M. E. Davis, *J. Catal.* **158**, 311 (1996).
- [7] F. Audry, P. E. Hoggan, J. Saussey, J. C. Lavalley, H. Lauron-Pernot, and A. M. Le Govic, *J. Catal.* **168**, 471 (1997).
- [8] A. I. Kingon, J.-P. Maria, and S. K. Streiffer, *Nature (London)* **406**, 1032 (2000).
- [9] M. Copel, M. Gribelyuk, and E. Gusev, *Appl. Phys. Lett.* **76**, 436 (2000).
- [10] C. Y. Lin, C. Y. Wu, C. Y. Wu, T. C. Lee, F. L. Yang, C. Hu, and T. Y. Tseng, *IEEE Electron Dev. Lett.* **28**, 366 (2007).
- [11] R. Huang, X. Yan, S. Ye, R. Kashtiban, R. Beanland, K. A. Morgan, M. D. B. Charlton, and C. H. de Groot, *Nanoscale Res. Lett.* **12**, 384 (2017).
- [12] S. I. Klokishner, O. Reu, C. E. Chan-Thaw, F. C. Jentoft, and R. Schlögl, *J. Phys. Chem. A* **115**, 8100 (2011).
- [13] H. Li, J.-I. J. Choi, W. Mayr-Schmölzer, C. Weilach, C. Rameshan, F. Mittendorfer, J. Redinger, M. Schmid, and G. Rupprechter, *J. Phys. Chem. C* **119**, 2462 (2015).
- [14] G. Bakradze, L. P. H. Jeurgens, and E. J. Mittemeijer, *J. Phys. Chem. C* **115**, 19841 (2011).
- [15] A. Christensen and E. A. Carter, *Phys. Rev. B* **58**, 8050 (1998).
- [16] M. Youssef, M. Yang, and B. Yildiz, *Phys. Rev. Appl.* **5**, 014008 (2016).
- [17] S. T. Korhonen, M. Calatayud, and A. O. I. Krause, *J. Phys. Chem. C* **112**, 6469 (2008).
- [18] M.-H. Chen, J. C. Thomas, A. R. Natarajan, and A. Van der Ven, *Phys. Rev. B* **94**, 054108 (2016).
- [19] A. S. Foster, V. B. Sulimov, F. Lopez Gejo, A. L. Shluger, and R. M. Nieminen, *Phys. Rev. B* **64**, 224108 (2001).
- [20] B. Puchala and A. Van der Ven, *Phys. Rev. B* **88**, 094108 (2013).
- [21] M. Youssef and B. Yildiz, *Phys. Rev. B* **89**, 024105 (2014).
- [22] J. P. Abriata, J. Garcés, and R. Versaci, *Bull. Alloy Phase Diagrams* **7**, 116 (1986).
- [23] A. S. Foster, A. L. Shluger, and R. M. Nieminen, *Phys. Rev. Lett.* **89**, 225901 (2002).
- [24] M. Youssef and B. Yildiz, *Phys. Rev. B* **86**, 144109 (2012).
- [25] G. Henkelman, B. P. Uberuaga, and H. Jónsson, *J. Chem. Phys.* **113**, 9901 (2000).
- [26] G. Kresse and J. Hafner, *Phys. Rev. B* **47**, 558 (1993).
- [27] G. Kresse and J. Hafner, *Phys. Rev. B* **49**, 14251 (1994).
- [28] G. Kresse and J. Furthmüller, *Comput. Mater. Sci.* **6**, 15 (1996).
- [29] G. Kresse and J. Furthmüller, *Phys. Rev. B* **54**, 11169 (1996).
- [30] J. P. Perdew, K. Burke, and M. Ernzerhof, *Phys. Rev. Lett.* **77**, 3865 (1996).
- [31] J. P. Perdew, K. Burke, and M. Ernzerhof, *Phys. Rev. Lett.* **78**, 1396 (1997).
- [32] J. Yang, M. Youssef, and B. Yildiz, *Phys. Chem. Chem. Phys.* **19**, 3869 (2017).
- [33] A. R. Allnatt and A. B. Lidiard, *Atomic Transport in Solids* (Cambridge University Press, Cambridge, 2003).
- [34] D. T. Gillespie, *J. Comput. Phys.* **22**, 403 (1976).
- [35] A. Einstein, *Investigations on the Theory of Brownian Movement* (Dover Publications, New York, 1956).
- [36] See Supplemental Material at <http://link.aps.org/supplemental/10.1103/PhysRevB.97.024114> for additional details of calculating diffusivity from kMC simulation.
- [37] J. Xue, *J. Electrochem. Soc.* **138**, 36C (1991).
- [38] K. Momma and F. Izumi, *J. Appl. Crystallogr.* **44**, 1272 (2011).
- [39] J. Greer, A. Korkin, and J. Labanowski, *Nano and Giga Challenges in Microelectronics* (Elsevier, Amsterdam, 2003).
- [40] B. Cox, *J. Nucl. Mater.* **336**, 331 (2005).